PAPER

Check for updates

Intraoperative diagnosis of early lymphatic metastasis using neodymium-based rare-earth NIR-II fluorescence nanoprobe†

Guangxin Duan,‡[c] Jingyu Zhang,‡[c] Zhuxin Wei,‡[ad] Ximing Wang,[b] Jianfeng Zeng, [iD][ce] Shuwang Wu,[c] Chunhong Hu*[b] and Ling Wen [iD] *[ab]

The high mortality of breast cancer is closely related to lymph node (LN) metastasis. Sentinel LNs (SLNs) are the first station where tumor cells metastasize through the lymphatic system. As such, achieving precise diagnosis of the early metastatic status of SLNs during surgery is of paramount importance for precision therapy of breast cancer. While invasive SLNs biopsy is the gold standard for evaluating the status of SLNs, its use is often time-consuming and may increase the risk of operation. It is still challenging to develop a means for rapid SLN metastasis diagnosis. Herein, $NaGdF_4$:5%Nd@$NaLuF_4$ rare earth nanoparticles (Gd:Nd-RENPs) with near-infrared-II (NIR-II) fluorescence and magnetic resonance imaging (MRI) properties were fabricated. With the nanoprobe, metastatic SLNs and lymph vessels (LVs) rapidly brighten and can be observed by the NIR-II imaging system, which is totally different from normal LNs and LVs. The remarkable contrast observed *via* NIR-II imaging serves to swiftly delineate metastatic SLNs from normal ones, subsequently guiding precise surgical resection of metastatic LNs in just 10 minutes. Furthermore, the consistency between the results obtained *via* MRI and NIR-II imaging further validates the dependability of this nanoprobe as a diagnostic tool for metastatic SLNs. Additionally, the Gd:Nd-RENPs exhibited good biocompatibility *in vitro* and *in vivo*. In this study, we demonstrated the advantages and prospects of NIR-II imaging for intraoperative early SLN metastasis assessment and shed light on the potential of the dual-modal Gd:Nd-RENPs as a nanoprobe.

1. Introduction

Breast cancer, the leading malignancy in females, has the second highest mortality rate of all female tumors.[1] Metastasis is the main reason for the high mortality of breast cancer. Lymphatic metastasis is the most common method of metastasis in breast cancer patients; thus, the axillary lymph node (ALN) metastasis status is closely related to the outcome and prognosis of breast cancer patients.[2,3] Due to the high probability of lymph node (LN) metastasis, patients with early breast cancer commonly undergo mastectomy combined with axillary lymph node dissection (ALND) to prevent recurrence.[4] However, excessive ALND may induce a number of complications, such as lymphedema, axillary web syndrome, and upper limb movement range reduction, which seriously affect the postoperative quality of life of patients.[5] To minimize the incidence of lymphatic metastasis during tumor resection, sentinel lymph node biopsy (SLNB) is essential for evaluating the presence of early metastases in sentinel lymph nodes, the first lymph node that tumor cells drain into.[6–8] Following the results of the SLNB, ALND is performed only in patients who test positive for metastases in the SLNs, consequently reducing the occurrence of excessive ALND and its subsequent complications.[9] SLNB is now widely considered the gold standard in diagnosing lymphatic metastasis.[10] The drawback, however, is a long intraoperative time, which lengths the surgery time and increases the risk to the patients. Therefore, it is urgently needed to exploit a real-time imaging method that can accurately assess early SLNs metastases during surgery.

Optical imaging, which possesses the advantages of real-time dynamics imaging and diffraction-limited high spatial

[a]*Department of Radiology, Suzhou Dushu Lake Hospital, Dushu Lake Hospital Affiliated to Soochow University, Medical Centre of Soochow University, Suzhou, 215001, Jiangsu, China. E-mail: wenling@suda.edu.cn*

[b]*Department of Radiology, The First Affiliated Hospital of Soochow University, Suzhou 215000, China. E-mail: hch5305@163.com*

[c]*Center for Molecular Imaging and Nuclear Medicine, State Key Laboratory of Radiation Medicine and Protection, School for Radiological and Interdisciplinary Sciences (RAD-X), Soochow University, Collaborative Innovation Center of Radiological Medicine of Jiangsu Higher Education Institutions, Suzhou 215123, China*

[d]*Department of MRI, Fuwai Hospital, National Center for Cardiovascular Diseases, Chinese Academy of Medical Sciences, Peking Union Medical College, Beijing 100037, China*

[e]*Suzhou Xinying Biomedical Technology Co. Ltd., Suzhou 215123, China*

† Electronic supplementary information (ESI) available. See DOI: https://doi.org/10.1039/d3na00254c

‡ These authors contributed equally.

resolution, is widely used in the areas of basic medicine and laboratory medicine.[11–14] However, traditional optical imaging, distinguished by their limited tissue penetration and signal-to-noise ratio (SNR), restrict their applications for *in vivo* imaging. In the past few years, optical imaging in the near-infrared (NIR) region has attracted extensive attention from researchers due to its advantages in penetration and SNR.[15,16] A U.S. Food and Drug Administration (FDA)-approved NIR probe, indocyanine green (ICG), has been successfully utilized in clinical settings for tumor navigation and lymph node imaging during surgery.[17–19] However, it still suffers from the limitation of tissue penetration depth (1–2 millimeters) and fluorescence fidelity in deep tissue.[20] Thus, imaging in the NIR-II region (900–1700 nm), which has a deeper tissue penetration depth (up to 9 millimeters)[21] and a higher fluorescence fidelity and SNR, shows extensive application prospects in intraoperative resection navigation,[22,23] vascular system imaging,[24,25] and lymphatic system imaging.[26,27] Correspondingly, the investigation and development of NIR-II nanoprobes is currently a research area of great interest and attention. Currently, a plethora of NIR-II nanoprobes, including organic small molecules,[28] quantum dots (QDs),[29,30] single-walled carbon nanotubes (SWCNTs)[31,32] and rare earth nanoparticles (RENPs),[33] have been widely reported. In particular, RENPs are attractive due to their excellent photostability and biocompatibility.[34] Therefore, RENPs are potential *in vivo* NIR-II imaging probes, especially for application in lymphatic diseases. In Cheng's study, RENPs@Lips were applied for lymphatic imaging, and their results showed that inguinal LNs can be resected completely under NIR-II imaging guidance after RENPs@Lips injection.[23] In addition, Tian and coworkers detected popliteal and sacral LNs and performed LNs biopsy and dissection by using liposome-coated lanthanide nanoparticles.[35] Those studies indicate the tremendous potential of RENPs for LNs imaging and guided LNs dissection. However, accurately assessing early SLN metastasis status by using RENPs is still challenging, and few studies have focused on this issue, although RENPs have the potential to replace SLNB and significantly shorten surgical time.

Keeping this idea in mind, rare-earth core/shell downshifting NaGdF$_4$:5%Nd@NaLuF$_4$ rare earth nanoparticles (Gd:Nd-RENPs) possessing excellent NIR-II fluorescence performance at approximately 1060 and 1340 nm were fabricated. The Gd:Nd-RENPs exhibit a higher SNR and clearer lymph vessels (LVs) imaging than commercial ICG. Subsequent *in vivo* real-time imaging showed that the fluorescence signals in normal LNs and LVs are weaker at first and increase over time. In contrast, metastatic LNs and LVs rapidly brighten, and then they attenuate gradually. The difference facilitates distinguishing metastatic SLNs from normal SLNs and guiding surgery for metastatic LN removal. Mechanistically, we speculate that the expansion of LVs caused by LN metastasis of tumor cells may be responsible for what we detected, which shows the rapid imaging of the nanoprobe in metastatic LNs. Overall, these findings shed light on the clinical application potential of Gd:Nd-RENPs for early SLN metastasis imaging and intraoperative navigation.

2. Materials and methods

2.1. Materials and reagents

Gadolinium(III)chloride hexahydrate (GdCl$_3$·6H$_2$O, 99.9%), lutetium(III)chloride hexahydrate (LuCl$_3$·6H$_2$O, 99.99%), neodymium(III)chloride hexahydrate (NdCl$_3$·6H$_2$O, 99.9%), sodium fluoride (NaF, 99.99%), sodium hydroxide (NaOH, 96%), oleic acid (OA, 85%), 1-octadecene (ODE, 90%) and chlorophosphonazo III were obtained from Shanghai Aladdin Co. Ltd. (Shanghai, China). Methyl thiazolyl tetrazolium (MTT) and dimethyl sulfoxide (DMSO) were purchased from Beijing Chemical Reagents Co. Ltd. (Beijing, China). Analytical-grade tetrahydrofuran (THF) was purchased from Titan Scientific Co. Ltd. (Shanghai, China). Polyethylene glycol (PEG) with a diphosphate group and a methoxy group (CH$_3$O–PEG–DP, M_w: 2000) at two ends was a customized product provided by Beijing Oneder-hightech Co. Ltd. (Beijing, China). All reagents were used as received without any purification.

2.2. Synthesis of NaGdF$_4$:5%Nd@NaLuF$_4$ core/shell nanoparticles

Monodispersed ultrasmall lanthanide fluoride nanocluster [NaLnF$_4$ (Ln = Gd/Nd, Lu)] precursors were synthesized through the classic liquid–solid–solution (LSS) strategy.[36,37] Briefly, 1.2 g of sodium hydroxide, 4 mL of deionized water, 9 mL of ethanol, and 20 mL of OA were successively added to a 50 mL flask and then stirred for 10 min. Afterward, 1 mL of a gadolinium chloride hexahydrate (0.475 mol L^{-1}) and neodymium chloride hexahydrate (0.025 mol L^{-1}) mixture aqueous solution was added to 4 mL of a sodium fluoride solution (0.5 mol L^{-1}) and stirred for 60 min to fabricate NaGdF$_4$:5%Nd. The NaLuF$_4$ nanoclusters (0.5 mol L^{-1}) were prepared in the same way. The resultant nanoclusters were dispersed in cyclohexane (2 mL) for further use. Subsequently, the NaGdF$_4$:5%Nd solution was added to a three-necked flask containing 6 mL OA and 10 mL ODE. The mixture was purged with nitrogen (N$_2$) at 70 °C for 30 min to remove the cyclohexane, heated to 280 °C and reacted for 30 min under stirring. After cooling to room temperature, the reaction solution was added to 2 mL of NaLuF$_4$ (0.5 mmol) nanocluster solution, 6 mL of OA and 10 mL of ODE and stirred for 60 min to fabricate OA-coated NaGdF$_4$:5%Nd@NaLuF$_4$ core/shell nanoparticles (Gd:Nd-RENPs).

PEG–diphosphate ligand (DP–PEG$_{2000}$) and OA-coated core/shell Gd:Nd-RENPs were added to 5 mL THF at a mass ratio of 10 : 1. The ligand exchange was then executed under stirring at 40 °C for 24 h. Then, the PEG-coated particles were precipitated by cyclohexane, washed with cyclohexane three times, and dried in a vacuum at room temperature for 2 h. Finally, 5 mL of Milli-Q water was added to dissolve the PEG-modified nanoparticles for further use.

2.3. Characterization of Gd:Nd-RENPs

The size and morphology of the nanoparticles were observed through an FEI Tecnai G20 transmission electron microscope (TEM). The concentration of Gd^{3+} was measured by inductively coupled plasma-mass spectrometry (ICP-MS). The

downconversion fluorescence spectra were characterized by FLS980 spectra equipped with an 808 nm laser. The longitudinal relaxivity (r_1) of Gd:Nd-RENPs was measured by a 3 tesla MRI scanner (MR Solution, UK). T_1 maps were calculated by pixelwise fitting of the TR-dependent signal intensity changes to a single exponential function.

2.4. Mouse lymphatic metastasis model

Specific pathogen-free (SPF)-grade nude female mice (5 weeks old) were purchased from Cavens Lab Animal Co., Ltd. (Changzhou, China) and fed adaptively for one week before tumor bearing. A lymphatic metastasis model was established by injecting $4T_1$ cells (5×10^5 in 25 μL PBS) into the left foot pad of mice. The model was detected by touching enlarged lymph nodes and histological analysis on day 7 postinjection.

All animal procedures were performed in accordance with the Guidelines for Care and Use of Laboratory Animals of Soochow University and approved by the Animal Ethics Committee of Soochow University.

2.5. NIR-II fluorescence imaging

The real-time imaging procedure started once 50 μL Gd:Nd-RENPs (1.0 mg mL^{-1}) were simultaneously injected into the bilateral paws of anesthetized model mice through venous catheters. Images were acquired via a 1000 nm long-pass filter and exposure time 300 ms at various time points postinjection to visualize both sides' lymphatic vessels and lymph nodes under excitation with an 808 nm laser at a power density of 45 mW cm^{-2}. Imaging of ICG was performed by using an 880 nm long-pass filter with exposure time 200 ms, at various time points following 50 μL ICG (0.1 mg mL^{-1}) injections.

After identifying the metastatic sentinel lymph nodes, the lymph nodes were precisely resected under the guidance of NIR-II imaging. After anesthetization, a 0.5–1 cm^2 incision was made above the lymph nodes, and the lymph nodes were subsequently resected under irradiation with an 808 nm laser. The incision was sutured, and the removed lymph nodes were fixed in 4% paraformaldehyde. Subsequently, standard processing procedures, including paraffin embedding, cutting into slices, and deparaffinization, were executed. Hematoxylin & eosin (H&E) staining and immunofluorescent staining of CD11b and DAPI were carried out. Finally, the slices were detected and recorded by optical microscopy (Leica DMI8) and laser scanning confocal microscopy (Olympus FV1200). Regarding rare earth staining, tissue slices were subjected to chlorophosphonazo III staining solution (chlorophosphonazo III, 20 mg L^{-1}, HNO$_3$, 0.03 mol L^{-1}) for 15 minutes at room temperature. After undergoing three thorough washes with ultra-pure water, the slices were sealed with neutral balsam and subsequently observed and documented via optical microscopy.

2.6. In vivo MRI

MRI was performed with a 3 tesla MRI scanner (MR Solution, UK) at 0, 1, 5, 8, 10, 15, 20, 25, 30, 45, 60, 75, 90, 105, and 120 min after Gd:Nd-RENPs (50 μL, 1.0 mg mL^{-1}) administration. T_1-weighted images were obtained by using a fast spin-
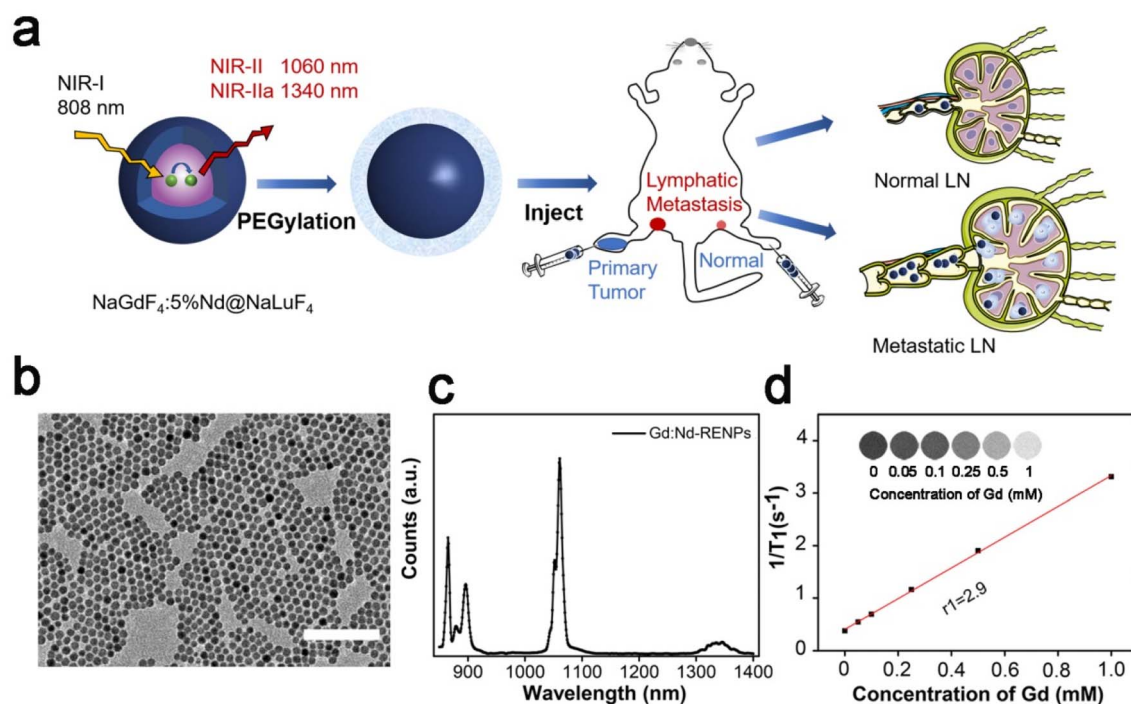

Fig. 1 Characterizations of NaGdF$_4$:5%Nd@NaLuF$_4$ NPs. (a) Schematic illustration of Gd:Nd-RENPs fabrication and lymphatic system imaging. (b) TEM image of Gd:Nd-RENPs (scale bar, 100 nm). (c) Downconversion photoluminescence spectrum of Gd:Nd-RENPs under an 808 nm excitation laser. (d) T_1 relaxivity plot of the aqueous suspension of Gd:Nd-RENPs.

echo sequence with fat saturation (TR/TE = 850/11 ms, FA = 90, FOV = 40). Images were analyzed by ImageJ software.

2.7. Biocompatibility evaluation

The cytotoxicity of Gd:Nd-RENPs in $4T_1$ and RAW 264.7 cells was assessed by MTT assays according to our previous studies.[38] Briefly, $4T_1$ and RAW 264.7 cells were seeded into 96-well plates and cultured in an incubator (37 °C, 5% CO_2) for 24 h. Then, 100 μL of media containing different concentrations of Gd^{3+} (0, 25, 50, 100, 200, 400, and 600 μg mL^{-1}) were added to each well and incubated for the other 24 h. Afterward, fresh media containing MTT (500 μg mL^{-1}) were added to the cells and incubated at 37 °C for 4 h. Thereafter, media containing MTT were discarded and replaced with 100 μL of DMSO. Following 15 min of shaking, the

absorbance at 490 nm was collected by a microplate reader (Biotek Synergy Neo 2) to calculate cell viability. For H&E staining, first, major organs were removed and fixed in 4% paraformaldehyde solution after mice were sacrificed at day 7 post Gd:Nd-RENPs administration at a dose of 15 mg kg^{-1}. Then, embedding with paraffin, cutting into slices and staining with H&E solution were carried out step by step. Finally, pathological slices were detected and recorded by a Leica DMI8 microscope.

2.8. Statistical analysis

Data are given as the mean ± standard deviation (SD). Statistical analysis was performed using a two-tailed Student's t-test.
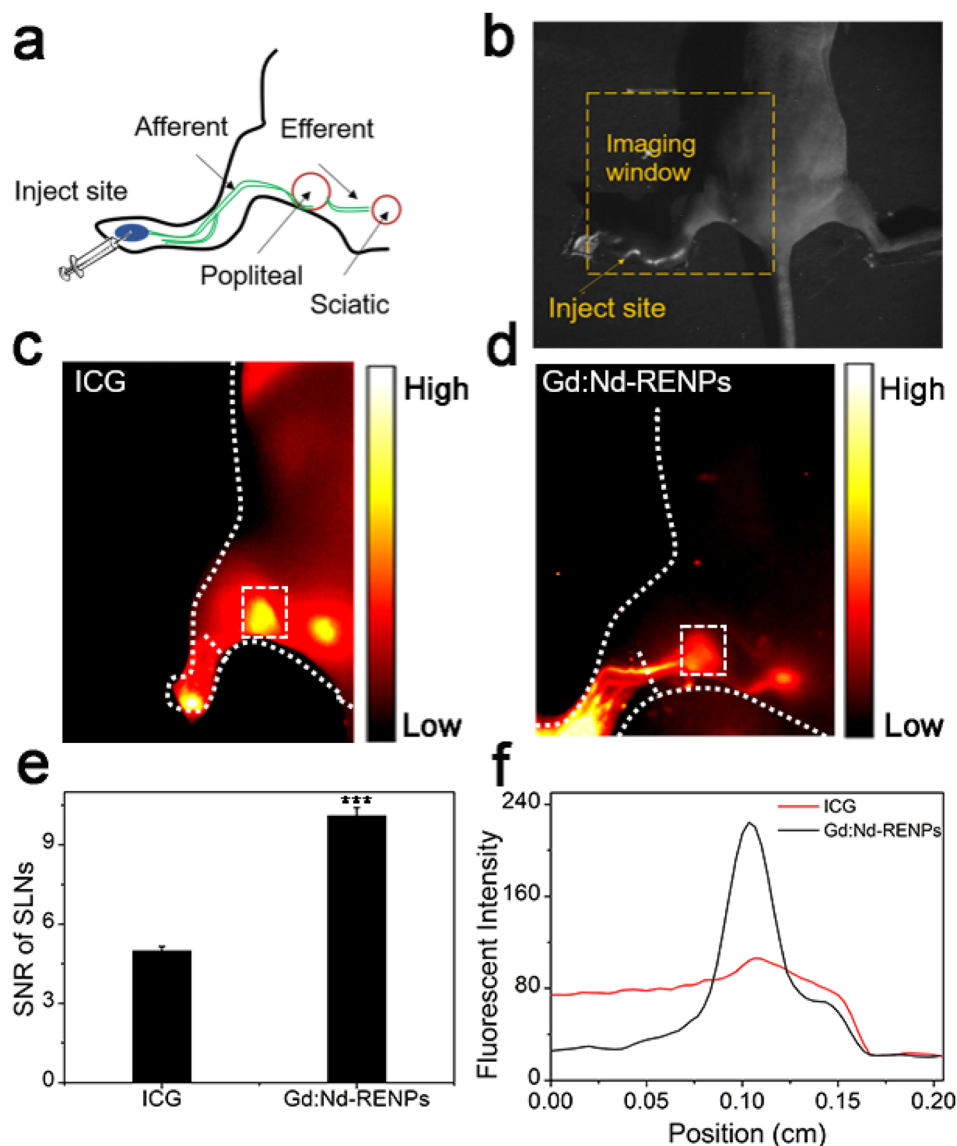

Fig. 2 Gd:Nd-RENPs enable high-contrast metastatic LN imaging. (a) Schematic illustration of the lymphatic system in the hindlimb of nude mice. The fluorescence probes were injected into the footpads. (b) Mouse setting position for NIR-II imaging and the imaging window. (c and d) Comparison of popliteal and sacral LNs imaging with Gd:Nd-RENPs in the NIR-II window and ICG in the NIR-I window, respectively, at 30 min after probes injection. (e) SNR of SLNs analyzed based on the signals in white dashed box after ICG and Gd:Nd-RENPs administration. (f) FWHM width and fluorescence intensity of LNs and LVs, based on the cross-sectional profiles [white lines in (c and d)].

Statistical significance was assigned for a p value < 0.05. *p < 0.05, **p < 0.01, ***p < 0.001.

3.   Results and discussion

3.1.   Synthesis and characterization of Gd:Nd-RENPs

The protocol of core/shell Gd:Nd-RENPs synthesis was similar to that we have reported previously.[38] TEM images showed that the NPs were spherical with regular morphology and uniform size. The average diameter was approximately 14.4 ± 2.1 nm (Fig. 1b and S1a†). The UV-vis-NIR absorption spectrum of the Gd:Nd-RENPs showed multiple absorption peaks in the region of 500–900 nm with a maximum absorbance peak between 790 and 810 nm, making the Gd:Nd-RENPs suitable for *in vivo* imaging under irradiation with an 808 nm laser (Fig. S1b†).[39] Due to the doping of Nd^{3+}, the Gd:Nd-RENPs exhibited two sharp emission peaks at 1060 and 1340 nm (Fig. 1c). The observation that the fluorescence intensity of the Gd:Nd-RENPs remained constant for 5 days underscores the high degree of photostability of these nanoparticles in both H_2O and PBS (Fig. S1c†), which confers considerable advantages for their potential use in biomedical applications. This enhanced photostability may be attributed to the success of the ligand exchange process (Fig. S2†). In addition to the bright photoluminescence in the NIR-II region, the Gd:Nd-RENPs exhibit interesting magnetism due to the presence of a large amount of

$NaGdF_4$ in the NPs.[40] The longitudinal proton relaxation time (T_1) relaxivity coefficient of the Gd:Nd-RENPs was measured *via* an MRI scanner under a 3 T magnetic field. As shown in Fig. 1d, $1/T_1$ was linearly dependent on the concentration of Gd^{3+}, and the r_1 value of the Gd:Nd-RENPs was 2.9 mM^{-1} s^{-1}, which is significantly higher than the value (1.09 mM^{-1} s^{-1}) we reported in our previous study,[38] which may be attributed to the more suitable sizes.[41] The NIR-II fluorescence property and relaxation performance indicate the potent potential of Gd:Nd-RENPs for *in vivo* imaging.

3.2.   NIR-II fluorescence imaging of LNs using Gd:Nd-RENPs and ICG

The excellent fluorescence property of the Gd:Nd-RENPs encouraged us to explore the NIR-II imaging effect of the NPs on metastatic LNs. To better assess the application potential of the NPs, we selected ICG as the control agent because ICG has been applied for LN imaging in LN dissection.[42,43] After ICG and Gd:Nd-RENPs administration (Fig. 2a) for 30 min, imaging was executed as shown in Fig. 2b. The results shown in Fig. 2c and d depict that both ICG and Gd:Nd-RENPs can image metastatic LNs clearly under 808 nm laser excitation. Furthermore, despite the fact that ICG results in a stronger fluorescence intensity within metastatic SLNs, Gd:Nd-RENPs imaging produces a more optimal SNR (10.1 ± 0.3) when compared to ICG (5.0 ± 0.2) (Fig. 2e), which results from the severe photobleaching of
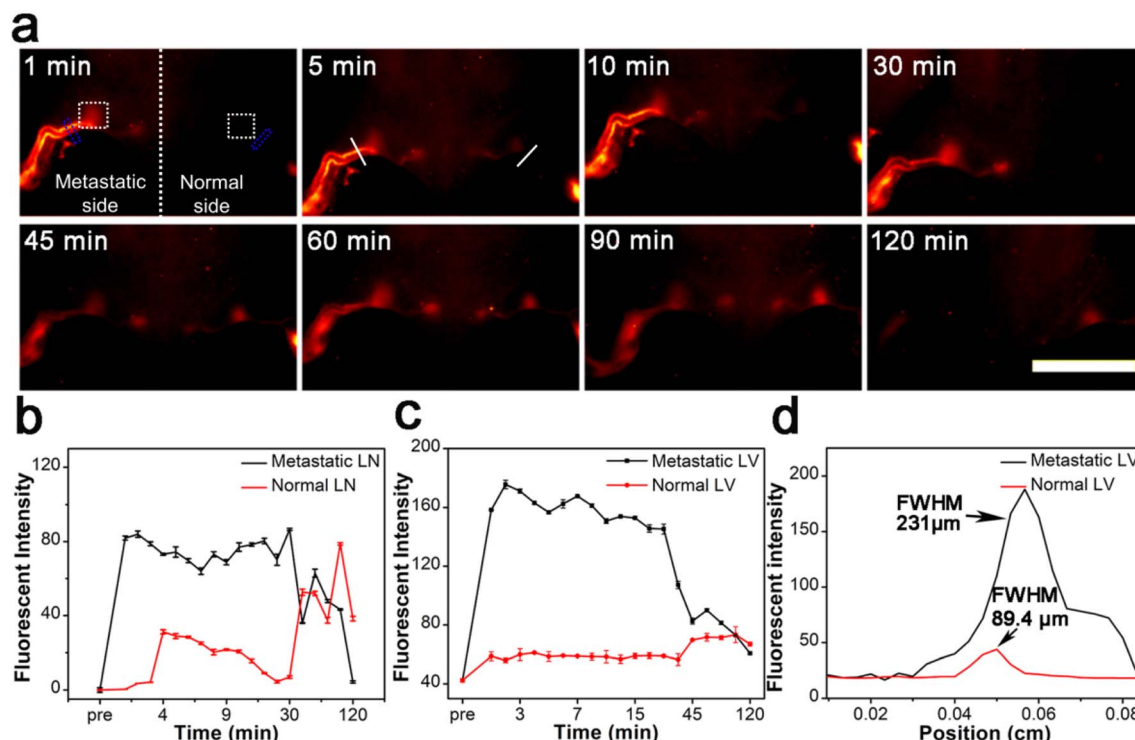

Fig. 3 NIR-II fluorescence imaging in normal and metastatic lymphatic systems using Gd:Nd-RENPs. (a) NIR-II fluorescence images of normal and metastatic popliteal LNs at different time points after injection of Gd:Nd-RENPs. Scale bar: 10 mm. (b) The fluorescence signal intensity (in white dashed box) of metastatic and normal LNs at different time points, $n = 3$. (c) The fluorescence signal intensity (in blue dashed box) of metastatic and normal LVs at different time points, $n = 3$. (d) The FWHM of metastatic and normal LVs at 5 min post-injection (signals were collected according to the white line in (a)).

ICG and its poorer tissue penetration compared to Gd:Nd-RENPs. Moreover, afferent LVs can be clearly observed (Fig. 2c, d and f) with the Gd:Nd-RENPs serving as the fluorescence probe, which may result from the special uptake of NPs by LVs.[44] The expansion of LVs has been found in many lymphatic metastasis patients and animal models, and has been proposed an indicator for the diagnosis of lymphatic metastasis.[45] Clear LVs imaging facilitates not only the pinpointing of SLNs but also the accurate evaluation of lymphatic metastasis. Thus, our results demonstrate that Gd:Nd-RENPs are superior to ICG for lymphatic imaging.

3.3. Real-time NIR-II imaging of metastatic and normal lymphatic systems

To further understand the imaging behavior of the Gd:Nd-RENPs, we compared the NIR-II fluorescence imaging behaviors of the Gd:Nd-RENPs between early-stage metastatic and normal lymphatic systems. As depicted in Fig. 3a, b and S3,† normal LNs are difficult to detect due to the weak fluorescence signals at the beginning of Gd:Nd-RENPs administration. Thereafter, the fluorescence signals slowly enhanced. The SLNs can be visualized clearly at 45 min, and the signals remain at 120 min without attenuation. In marked contrast, the metastatic SLNs brightened
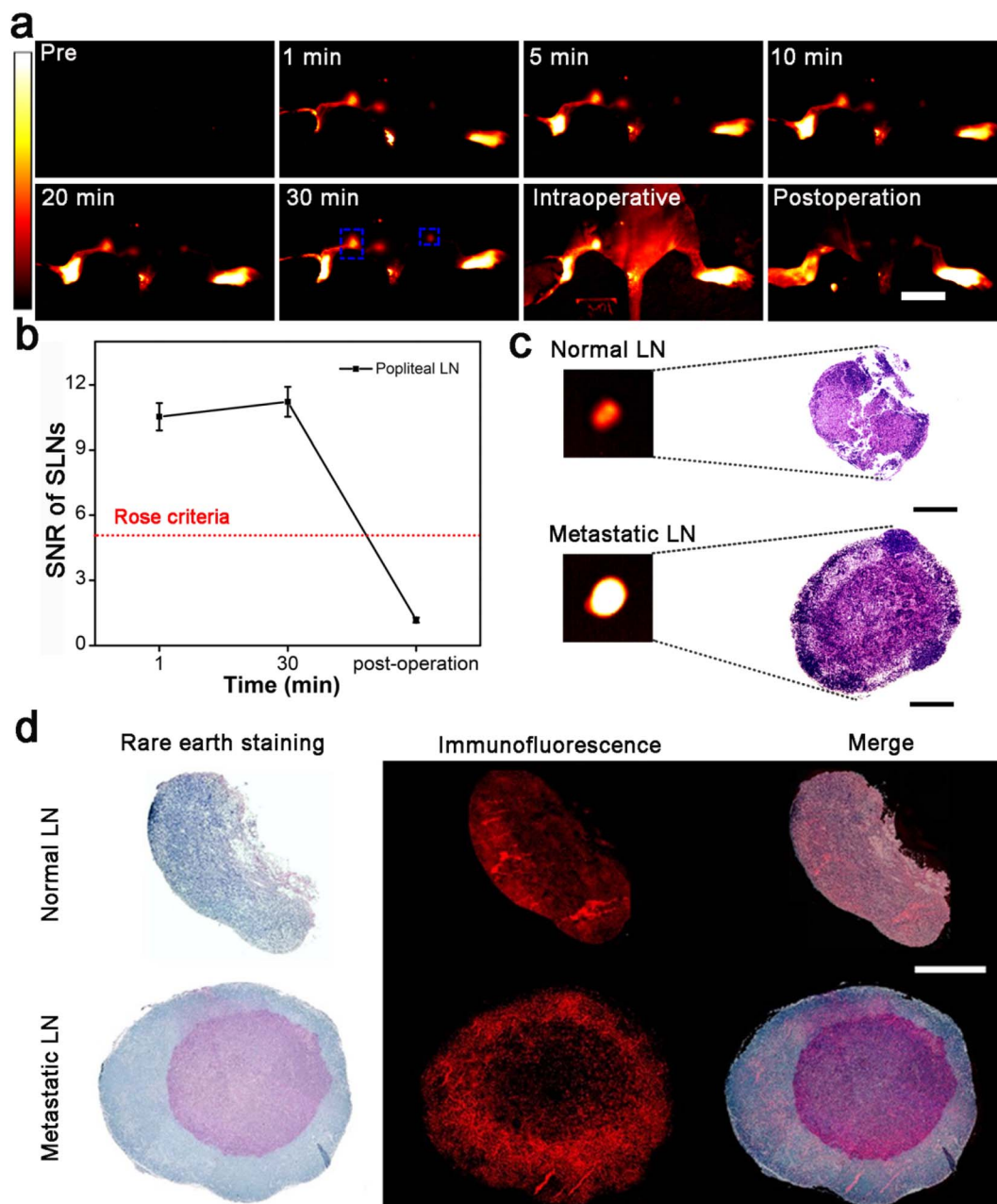

Fig. 4 SLN mapping and biopsy guidance by NIR-II imaging. (a) SLNs were localized and dissected under NIR-II image navigation (scale bar: 10 mm). (b) SNR of SLNs during surgery, $n = 3$. (c) Histological analysis of resected metastatic and normal LNs by H&E staining. (d) Photographs of normal and metastatic LNs after performing rare earth and CD11b^{+} immunofluorescence staining. Scale bar: 500 μm.

rapidly in 5 min, and the signal intensity was approximately 2.3 times stronger than that of the normal SLNs (Fig. 3a and b) at 5 min. The significant difference can distinguish metastatic SLNs from normal SLNs and guide the resection of metastatic SLNs. In parallel, a similar phenomenon of LVs imaging was observed. Unlike normal LVs, which display weak signals that increase gradually, the metastatic LVs lit up immediately after Gd:Nd-RENPs administration, and the signals were maintained for approximately 30 min, then began to attenuate sharply, and almost disappeared at approximately 120 min postinjection (Fig. 3a and c). The signal intensity of metastatic LVs was approximately 2.9 times stronger than that of normal LVs at 5 min. Additionally, the LVs on the metastatic side expanded significantly, and the full width at half maximum (FWHM) increased to 231 μm, which is approximately 2.6-fold greater than that of the normal LVs (Fig. 3a, c and d), providing additional evidence of lymphatic metastasis and facilitating diagnosis for doctors. Regarding the significant difference we observed by NIR-II imaging, it is rational to speculate that pathologic LN metastasis enlarges the inner diameter of LVs; therefore, the nanoprobe can rapidly fill up the afferent LVs, which manifests as the rapid and prolonged imaging of metastatic LVs and LNs. Additionally, advanced metastatic SLNs cannot be detected under NIR-II imaging with Gd:Nd-RENPs (Fig. S4†), which may be attributed to the lymphatic drainage obstruction caused by larger metastases.[45] Fortunately, later-stage metastatic SLNs can be easily diagnosed by MRI, which greatly reduces the probability of false-negatives during intraoperative metastatic SLN diagnosis.

3.4. SLN mapping and resection guided by NIR-II imaging

The clear lymphatic system imaging demonstrates that Gd:Nd-RENP injection is helpful to delineate LVs and LNs during surgery. Additionally, due to the appropriate imaging time difference between metastatic LNs and normal LNs, metastatic SLNs can be easily distinguished from normal SLNs with the help of Gd:Nd-RENPs. Herein, we mimicked the clinical surgery of metastatic LN dissection in model mice. Due to the fluorescence property of the Gd:Nd-RENPs in the NIR-II region, SNR of

metastatic SLNs reached >10 in the first 30 min after Gd:Nd-RENPs injection (Fig. 4a and b). Therefore, the metastatic SLNs were clearly observed and precisely dissected from surrounding tissue under irradiation with an 808 nm laser (Fig. 4a and b). Subsequently, NIR-II fluorescence imaging of resected normal and metastatic LNs was employed. As depicted in Fig. 4c, the signal of metastatic SLNs was much stronger than that of normal SLNs, which is consistent with the *in vivo* imaging results. Histological analysis confirmed that breast cancer metastasis existed in the SLN, and the contralateral LN was normal (Fig. 4c). Furthermore, we analyzed the distribution of Gd:Nd-RENPs in metastatic and normal SLNs. As Fig. 4d depicts, the rare earth elements (dyed blue) are predominantly located at the cortex and exhibit colocalization with CD11b$^+$ macrophages. These findings suggest that Gd:Nd-RENPs are primarily taken up by macrophages residing in the SLNs cortex. Similarly, in metastatic SLNs, rare earth signals are also detected in CD11b$^+$ macrophages, indicating that Gd:Nd-RENPs are endocytosed by macrophages present in both normal and metastatic SLNs, which is consistent with the observations made in Bennett's study.[46] In conclusion, within the 30 min surgical time window, metastatic LNs could be identified and resected rapidly and accurately under the navigation of NIR-II imaging with the aid of Gd:Nd-RENPs, which has the potential to replace intraoperative ALNB, thus greatly reducing surgery time.

3.5. MRI of SLNs

In addition to the NIR-II fluorescence property, the interesting magnetic properties of Gd:Nd-RENPs due to their containing Gd^{3+}, which can relax water protons, enables the probe to improve the contrast of LNs during perioperative MRI examination. As depicted in Fig. 5a and b, the signal of normal LNs (marked with the yellow arrow) increased significantly with time in the first 120 min. Moreover, the signal of metastatic SLNs (marked with the red arrow) reached the maximum in 5 min post Gd:Nd-RENP injection. Thereafter, the signals decreased gradually over time (Fig. 5a and S5†). These observations align entirely with the results of NIR-II imaging, further
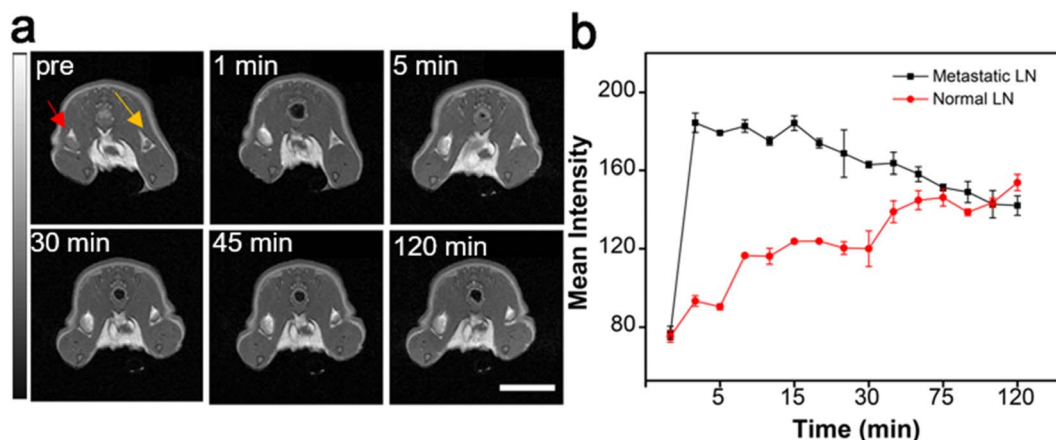

Fig. 5 *In vivo* MRI of LNs at different time points after Gd:Nd-RENPs injection. (a) T_1-weighted MRI of metastatic and normal SLNs after injection with Gd:Nd-RENPs (scale bar: 10 mm). (b) Mean intensity of MR signals of metastatic and normal SLNs against time, $n = 3$.
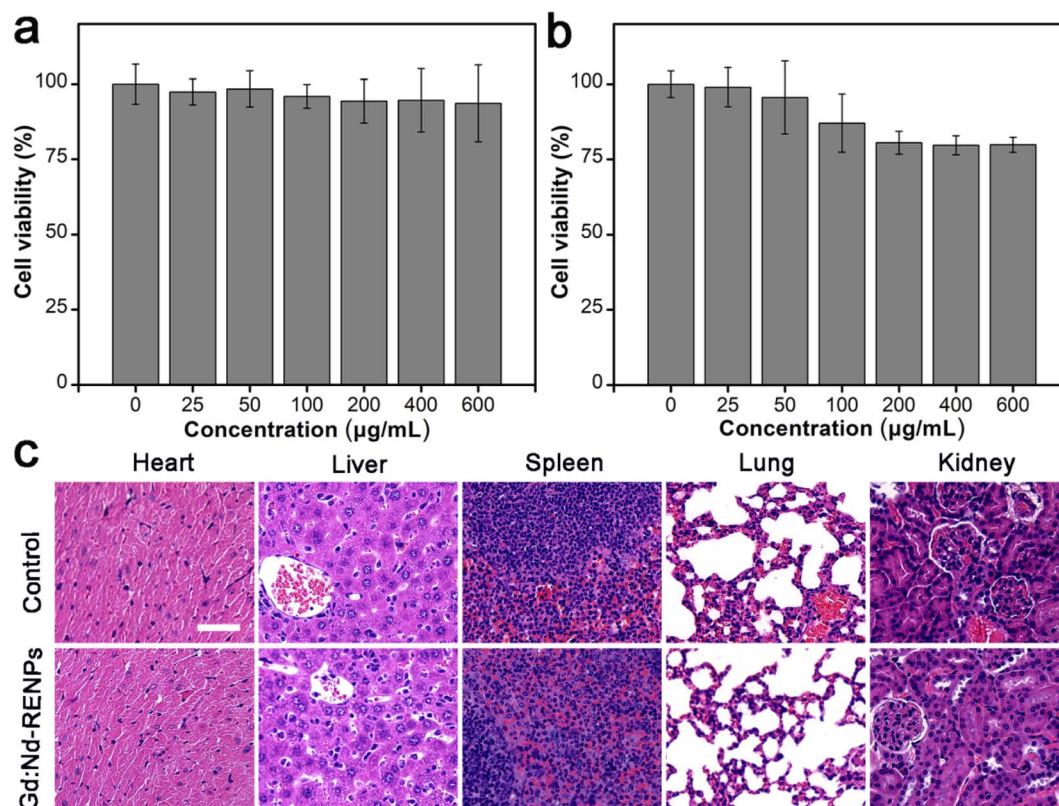
Fig. 6 *In vitro* and *in vivo* biocompatibility of Gd:Nd-RENPs. The cell viabilities of $4T_1$ (a) and Raw 264.7 (b) cells were evaluated by MTT assay after 24 h of treatment in media containing different concentrations of Gd:Nd-RENPs, $n = 6$. (c) *In vivo* biocompatibility was detected by H&E staining of major organs at day 7 post Gd:Nd-RENPs administration (15 mg kg^{-1}). Scale bar: 50 μm.

corroborating the trustworthiness of this imaging modality in accurately distinguishing between normal and metastatic SLNs.

3.6. Biocompatibility of Gd:Nd-RENPs

Additionally, the biocompatibility of Gd:Nd-RENPs was determined. Fig. 6a displays the cell viability of $4T_1$ and Raw 264.7 cells analyzed by MTT assay after exposure to different concentrations of Gd:Nd-RENPs for 24 h. Based on the results obtained, it can be inferred that Raw 264.7 cells possess a slightly greater sensitivity to Gd:Nd-RENPs when compared to $4T_1$ cells, a phenomenon potentially explained by the heightened endocytic capacity of the Raw 264.7 cells. The cell viability of Raw 264.7 cells exceeded 80%, even when the concentration of Gd^{3+} was as high as 600 μg mL^{-1}, reflecting the remarkable *in vitro* biocompatibility of the Gd:Nd-RENPs. Furthermore, the *in vivo* biocompatibility was observed by histopathological section (H&E staining) analysis. As shown in Fig. 6b, no obvious pathological injury was observed compared to the control group at day 7 postadministration, illustrating the good *in vivo* biocompatibility of the Gd:Nd-RENPs, as well as their potent potential for clinical application.

4. Conclusions

In this work, we have successfully synthesized a dual-modal rare-earth nanoprobe, Gd:Nd-RENPs. Due to their good

fluorescence property in the NIR-II region, Gd:Nd-RENPs enable high-SNR LNs imaging and high-quality LVs visualization, which is superior to that of commercial ICG. Additionally, with the help of NIR-II imaging, the early metastatic lymphatic system can be quickly distinguished from its normal counterpart without invasion due to their different imaging performances. Based on this, intraoperative metastatic SLNs identification and dissection were rapidly and accurately performed, exhibiting the potential of this approach for replacing traditional SLNB. In addition to its optical properties, the interesting magnetism of Gd:Nd-RENPs facilitates preoperative LN staging by MRI. MRI displayed a result consistent with that of NIR-II imaging. Moreover, the well-performing Gd:Nd-RENPs exhibited high *in vitro* and *in vivo* biocompatibility. Consequently, this study reveals that Gd:Nd-RENPs have great value for clinical application in the accurate diagnosis of early metastatic LNs and surgical resection under NIR-II imaging guidance.

Author contributions

Guangxin Duan: original draft writing, investigation; Zhuxin Wei: investigation, original draft writing, formal analysis; Jingyuan Zhang: investigation, formal analysis; Ximing Wang: review and editing, methodology; Jianfeng Zeng: review and editing, conceptualization; Shuwang Wu: review and editing;

Chunhong Hu: conceptualization, methodology, review and editing; Ling Wen: methodology, conceptualization, review and editing, project administration; Mingyuan Gao: conceptualization, project administration.

Conflicts of interest

The authors declare no competing financial interests.

Acknowledgements

References

1 R. L. Siegel, K. D. Miller and A. Jemal, *Ca-Cancer J. Clin.*, 2019, **69**, 7–34.

2 R. D. Neal, P. Tharmanathan, B. France, N. U. Din, S. Cotton, J. Fallon-Ferguson, W. Hamilton, A. Hendry, M. Hendry, R. Lewis, U. Macleod, E. D. Mitchell, M. Pickett, T. Rai, K. Shaw, N. Stuart, M. L. Torring, C. Wilkinson, B. Williams, N. Williams and J. Emery, *Br. J. Cancer*, 2015, **112**(suppl. 1), S92–S107.

3 B. Quinn, Z. Dauer, N. Pandit-Taskar, H. Schoder and L. T. Dauer, *BMC Med. Imaging*, 2016, **16**, 41.

4 E. Martin-Sanchez, E. Pernaut-Leza, S. Mendaza, A. Cordoba, F. Vicente-Garcia, I. Monreal-Santesteban, J. P. Vizcaino, M. J. De Cerio, N. Perez-Janices, I. Blanco-Luquin, D. Escors, A. Ulazia-Garmendia and D. Guerrero-Setas, *Virchows Arch.*, 2016, **469**, 51–59.

5 M. Trignani, C. Di Carlo, C. Cefalogli, M. Nuzzo, L. A. Ursini, L. Caravatta, F. Perrotti, M. Di Nicola, A. Pamio and D. Genovesi, *In Vivo*, 2017, **31**, 151–158.

6 A. E. Giuliano, K. V. Ballman, L. McCall, P. D. Beitsch, M. B. Brennan, P. R. Kelemen, D. W. Ollila, N. M. Hansen, P. W. Whitworth, P. W. Blumencranz, A. M. Leitch, S. Saha, K. K. Hunt and M. Morrow, *J. Am. Med. Assoc.*, 2017, **318**, 918–926.

7 N. Harbeck and M. Gnant, *Lancet*, 2017, **389**, 1134–1150.

8 P. L. Geoffrey and Y. E. Stanislav, *Radiology*, 2015, **277**, 1–8.

9 J. M. Ye, B. L. Guo, Q. Liu, F. Ma, H. J. Liu, Q. Wu, L. Xin, Y. J. Cheng, H. Zhang, S. Zhang, X. N. Duan, J. G. Zhang and Y. H. Liu, *China Med. J.*, 2021, **134**, 886–894.

10 S. A. Stacker, S. P. Williams, T. Karnezis, R. Shayan, S. B. Fox and M. G. Achen, *Nat. Rev. Cancer*, 2014, **14**, 159–172.

11 Y. Cai, Z. Wei, C. Song, C. Tang, W. Han and X. Dong, *Chem. Soc. Rev.*, 2019, **48**, 22–37.

12 P. Yan, T. Wang, D. Zhang and X. Ma, *Chin. J. Org. Chem.*, 2019, **39**, 916.

13 L. Xiong, Y. Fan and F. Zhang, *Acta Chim. Sin.*, 2019, **77**, 1239.

14 L. Yang, B. Liu, N. Li and B. Tang, *Acta Chim. Sin.*, 2017, **75**, 1047.

15 Y. Fan, P. Wang, Y. Lu, R. Wang, L. Zhou, X. Zheng, X. Li, J. A. Piper and F. Zhang, *Nat. Nanotechnol.*, 2018, **13**, 941–946.

16 P. Wang, Y. Fan, L. Lu, L. Liu, L. Fan, M. Zhao, Y. Xie, C. Xu and F. Zhang, *Nat. Commun.*, 2018, **9**, 2898.

17 A. L. Vahrmeijer, M. Hutteman, J. R. van der Vorst, C. J. van de Velde and J. V. Frangioni, *Nat. Rev. Clin. Oncol.*, 2013, **10**, 507–518.

18 Q. Y. Chen, J. W. Xie, Q. Zhong, J. B. Wang, J. X. Lin, J. Lu, L. L. Cao, M. Lin, R. H. Tu, Z. N. Huang, J. L. Lin, H. L. Zheng, P. Li, C. H. Zheng and C. M. Huang, *JAMA Surg.*, 2020, **155**, 300–311.

19 R. Souzaki, N. Kawakubo, T. Matsuura, K. Yoshimaru, Y. Koga, J. Takemoto, Y. Shibui, K. Kohashi, M. Hayashida, Y. Oda, S. Ohga and T. Taguchi, *Pediatr. Surg. Int.*, 2019, **35**, 551–557.

20 F. Ding, Y. Fan, Y. Sun and F. Zhang, *Adv. Healthcare Mater.*, 2019, **8**, 1900260.

21 J. Cao, B. Zhu, K. Zheng, S. He, L. Meng, J. Song and H. Yang, *Front. Bioeng. Biotechnol.*, 2020, **7**, 1–21.

22 Z. Hu, C. Fang, B. Li, Z. Zhang, C. Cao, M. Cai, S. Su, X. Sun, X. Shi and C. Li, *Nat. Biomed. Eng.*, 2019, 1–13.

23 D. Li, S. He, Y. Wu, J. Liu, Q. Liu, B. Chang, Q. Zhang, Z. Xiang, Y. Yuan, C. Jian, A. Yu and Z. Cheng, *Adv. Sci.*, 2019, **6**, 1902042.

24 B. Li, M. Zhao, L. Feng, C. Dou, S. Ding, G. Zhou, L. Lu, H. Zhang, F. Chen and X. Li, *Nat. Commun.*, 2020, **11**, 1–11.

25 Y. Li, D. Hu, Z. Sheng, T. Min, M. Zha, J.-S. Ni, H. Zheng and K. Li, *Biomaterials*, 2021, **264**, 120365.

26 D. Li, C. Qu, Q. Liu, Y. Wu, X. Hu, K. Qian, B. Chang, S. He, Y. Yuan and Y. Li, *Adv. Funct. Mater.*, 2020, **30**, 1906343.

27 R. Tian, H. Ma, S. Zhu, J. Lau, R. Ma, Y. Liu, L. Lin, S. Chandra, S. Wang and X. Zhu, *Adv. Mater.*, 2020, **32**, 1907365.

28 R. Sang, X. Xu, Q. Wang, Q. Fan and W. Huang, *Acta Chim. Sin.*, 2020, **78**, 901.

29 C. Li, Y. Zhang, M. Wang, Y. Zhang, G. Chen, L. Li, D. Wu and Q. Wang, *Biomaterials*, 2014, **35**, 393–400.

30 Y. Du, B. Xu, T. Fu, M. Cai, F. Li, Y. Zhang and Q. Wang, *J. Am. Chem. Soc.*, 2010, **132**, 1470–1471.

31 G. Hong, J. Lee, J. Robinson, U. Raaz, L. Xie, N. Huang, J. Cooke and H. Dai, *Nat. Med.*, 2012, **18**, 1841–1846.

32 G. Hong, S. Diao, A. L. Antaris and H. Dai, *Chem. Rev.*, 2015, **115**, 10816–10906.

33 D. J. Naczynski, M. C. Tan, M. Zevon, B. Wall, J. Kohl, A. Kulesa, S. Chen, C. M. Roth, R. E. Riman and P. V. Moghe, *Nat. Commun.*, 2013, **4**, 2199.

34 C. Li and J. Lin, *J. Mater. Chem.*, 2010, **20**, 6831–6847.

35 J. Yang, S. He, Z. Hu, Z. Zhang, C. Cao, Z. Cheng, C. Fang and J. Tian, *Nano Today*, 2021, **38**, 101120.

36 X. Wang, J. Zhuang, Q. Peng and Y. Li, *Nature*, 2005, **437**, 121–124.

37 F. Ren, H. Liu, H. Zhang, Z. Jiang, B. Xia, C. Genevois, T. He, M. Allix, Q. Sun, Z. Li and M. Gao, *Nano Today*, 2020, **34**, 100905.

38 Z. Wei, G. Duan, B. Huang, S. Qiu, D. Zhou, J. Zeng, J. Cui, C. Hu, X. Wang, L. Wen and M. Gao, *J. Nanobiotechnol.*, 2021, **19**, 369.

39 S. H. X. Zhang and B. Ding, *Chem. Eng.*, 2020, **385**, 123959.

40 J. Huang, Y. Hou, C. Liu, L. Jing, T. Ma, X. Sun and M. Gao, *Chem. Mater.*, 2015, **27**, 7918–7925.

41 H. Dong, S. R. Du, X. Y. Zheng, G. M. Lyu, L. D. Sun, L. D. Li, P. Z. Zhang, C. Zhang and C. H. Yan, *Chem. Rev.*, 2015, **115**, 10725–10815.

42 E. P. Mamounas, T. Kuehn, E. J. T. Rutgers and G. von Minckwitz, *Lancet*, 2017, **17**, 31451–31454.

43 Z. Starosolski, R. Bhavane, K. B. Ghaghada, S. A. Vasudevan, A. Kaay and A. Annapragada, *PLoS One*, 2017, **12**, e0187563.

44 C.-Y. Yu, P.-H. Huang, L. L.-C. Tsang, H.-W. Hsu, W.-X. Lim, C.-C. Weng, T.-L. Huang, C.-C. Hsu, C.-L. Chen and H.-Y. Ou, *J. Hepatocell. Carcinoma*, 2023, 17–26.

45 S. Karaman and M. Detmar, *J. Clin. Invest.*, 2014, **124**, 922–928.

46 Z. T. Bennett, Q. Feng, J. A. Bishop, G. Huang, B. D. Sumer and J. Gao, *Theranostics*, 2020, **10**, 3340–3350.